Atomically precise step grids for the engineering of helical states

J. Enrique Ortega [1,2,3,*] Guillaume Vasseur,[3] Frederik Schiller,[2] Ignacio Piquero-Zulaica [2] Andrew P. Weber,[3]
Julien Rault,[4] Miguel Angel Valbuena [5,6] Stefano Schirone [5] Sonia Matencio,[5] Leonid A. Sviatkin [3,7]
Daria V. Terenteva [3,7] Yury M. Koroteev [3,8,9] Evgueni V. Chulkov,[3,9,10]
Aitor Mugarza,[5,11,†,‡] and Jorge Lobo-Checa [12,13,†,§]

[1]*Departamento de Física Aplicada I, Universidad del País Vasco, 20018 San Sebastian, Spain*
[2]*Centro de Física de Materiales CSIC/UPV-EHU, Manuel Lardizabal 5, 20018 San Sebastian, Spain*
[3]*Donostia International Physics Centre, Manuel de Lardizabal 4, 20018 San Sebastian, Spain*
[4]*Synchrotron SOLEIL, L'Orme des Merisiers Saint-Aubin, F-91192 Gif-sur-Yvette Cedex, France*
[5]*Catalan Institute of Nanoscience and Nanotechnology (ICN2), CSIC and Barcelona Institute of Science and Technology,
Campus UAB, Bellaterra, 08193 Barcelona, Spain*
[6]*Instituto Madrileño de Estudios Avanzados, IMDEA Nanociencia, Calle Faraday 9, 28049 Madrid, Spain*
[7]*Tomsk Polytechnic University, 634050 Tomsk, Russia*
[8]*Institute of Strength Physics and Materials Science of SB RAS, 634055 Tomsk, Russia*
[9]*Saint Petersburg State University, 199034 Saint Petersburg, Russia*
[10]*Departamento de Física de Materiales, Universidad del País Vasco, 20018 San Sebastián, Spain*
[11]*ICREA - Institució Catalana de Recerca i Estudis Avançats, Lluis Companys 23, 08010 Barcelona, Spain*
[12]*Instituto de Nanociencia y Materiales de Aragón, CSIC-Universidad de Zaragoza, E-50009 Zaragoza, Spain*
[13]*Departamento Física de la Materia Condensada, Universidad de Zaragoza, E-50009 Zaragoza, Spain*

Conventional spin-degenerate surface electrons have been effectively manipulated by means of self-organized nano-arrays. Of particular interest are one-dimensional, step superlattices at vicinal surfaces, because their fundamental behavior can be understood through simple model theory, and they can be utilized to imprint strong surface anisotropies in electron transport devices. In this work, the realization of periodic resonator arrays on the $BiAg_2$ atom-thick surface alloy with atomic precision is presented, and their potential ability for tailoring the giant-split helical Rashba states is demonstrated. By employing curved crystals to select local vicinal planes, two sharply defined arrays of $BiAg_2$ monoatomic steps with distinct spacing are fabricated, as experimentally determined from scanning tunneling microscopy and low-energy electron diffraction. The interaction of the Rashba helical states with the step arrays is assessed by scanning the photon beam across the $BiAg_2$ curved surface in angle-resolved photoemission experiments and comparing these results with density functional theory. Remarkably, strong orbital-selective renormalization of bands perpendicular to the step superlattice, as well as spin mixing of Rashba bands, are induced by the coherent scattering of the periodic step potential. These results pave the way to fabricate atomically precise coupled arrays of electron resonators to engineer spin-orbital textures.

I. INTRODUCTION

Materials exhibiting Rashba spin-orbit coupling (SOC) have triggered immense research activity that led to the opening of a new field in spintronics, the so-called spin orbitronics [1–3]. As for any other material, their successful technological application depends on two factors: a fundamental understanding of the emerging phenomena, and the capability to engineer and tune their key properties. Exposing Rashba electrons to superlattice potentials is a very attractive approach

to simultaneously realize these two conditions. Indeed, the interaction of Rashba electrons with one-dimensional (1D) periodic potentials can induce standing spin waves [4] and spin-orbit density waves [5]. In the latter, the electric field induced spin accumulation can be altered selectively along the superlattice direction [6]. Moreover, this characteristic spin texture can be further manipulated using terahertz radiation [7]. Collective excitations such as plasmons also exhibit a similar anisotropic tunability [8]. Recently, the use of periodic potentials has been proposed as a scaffold to engineer the topology of Rashba superconductors aiming at the generation of Majorana fermions [9,10].

From a fundamental perspective, the renormalization of the spin-orbital texture behind the aforementioned phenomena can be unraveled using 1D self-assembled step superlattices. In conventional metal [11–13] and semiconductor [14,15]

---
*Corresponding author: enrique.ortega@ehu.es
†These authors contributed equally to this work.
‡Corresponding author: aitor.mugarza@icn2.cat
§Corresponding author: jorge.lobo@csic.es

surfaces, such step arrays have been successfully employed as coupled resonator systems capable of tuning the overall electron confinement [12,16], as well as for finding the coupling between the electronic and elastic energies of these nanostructures [17,18]. Adding the characteristic Rashba-type spin-momentum locking to surface electrons, the emergence of new scattering mechanisms is expected, which in the presence of 1D periodic structures could give rise to exotic band renormalization, in a similar way to the one observed for pseudospin-momentum locked electrons in graphene [19]. The effect of vicinality on the native Shockley state of the Au(111) surface does not change the spin polarization and texture of this state due to the weak SOC and pure nondegenerate orbital composition [20]. Delving into systems with stronger spin-orbit interaction would be desirable. For instance, coupling of Rashba states of 1D Pb nanostripes has been achieved using Si vicinal surfaces as templates [21,22]. In these systems, the appropriate selection of the vicinal plane and Pb doping can result in Fermi surface nesting of their Rashba bands with the same spin helicity, leading to a spin-orbit density wave [5,23]. However, the interaction of these terrace-confined Pb nanowires with adjacent steps is considerably weaker than for the two-dimensional (2D) Rashba electron gas of the monolayer $BiAg_2$ alloy [24–28]. In addition to the strong interterrace coupling, the $BiAg_2$ monolayer also exhibits a complex spin-orbital texture that, combined with the chemical heterogeneity of the steps, gives rise to an anisotropic spin-flip scattering mechanism [25]. Implementing highly ordered step arrays on $BiAg_2$, or any other relevant 2D SOC systems, is thereby very desirable, as novel emergent SOC related intriguing phenomena are to be expected. Despite the great technological potential bestowed, its realization and control still remain a challenge to date.

Here we demonstrate that the fabrication of atomically sharp $BiAg_2$ step superlattices with variable periodicity is feasible. Following scanning tunneling microscopy (STM) imaging and low-energy electron diffraction (LEED), we find particularly stable, straight step arrays spaced with atomic precision at specific azimuthal directions, revealing the stabilizing role of the basic surface alloy structure. Moreover, two local planes on the curved surface match the integer number of the $BiAg_2$ alloy unit cell, which result on unimodal, atomically sharp superlattices. We investigate the helical Rashba states on such "magic" planes via angle-resolved photoemission spectroscopy (ARPES) [11,17,18,29]. We observe coherent scattering of Rashba-split bands at the step arrays, which results in an orbital-selective renormalization of the bands in the direction perpendicular to the steps that leads to a profound modulation of the in-plane orbital dichroism. We gain insight into these experimental results by means of density functional theory (DFT), which reveals that the interaction of Rashba electrons with the step superlattice also drives a reorientation of the spin texture in both parallel and perpendicular directions.

II. RESULTS

The $BiAg_2$ monolayer alloy can be readily grown on Ag(111), although its synthesis on vicinal Ag(111) surfaces has not been explored. In Fig. 1 we show that the

deposition of 0.33 monolayer (ML) of Bi at 300 K followed by post-annealing to 550 K leads to atomic quality and accurate $BiAg_2$ stoichiometry within (111) terraces of vicinal surfaces, but the particular step geometry of the substrate influences step-lattice order. Different step morphologies are experimentally accessed by selecting the axis of the cylindrical crystal sector, that is, the step direction [Fig. 1(a)]. For a curved crystal featuring close-packed steps [c-Ag(111)$_{cp}$ sample], we do not achieve the desired structural ordering of the step lattice, as shown in Figs. 1(b) and 1(c) (see Fig. S1 in the Supplemental Material for a complete set of STM pictures [30]). On the terraces one can resolve the characteristic $(\sqrt{3} \times \sqrt{3})R30°$ atomic structure of the Bi sublattice, but steps exhibit irregular sawlike terminations that reconstruct in a 120° zigzagged geometry forming alternate segments of fully kinked steps along [11$\bar{2}$] and [$\bar{2}$11] [cf. Fig. 1(b)]. As schematically overlaid using the atomic model of Fig. 1(c), the zigzag step roughening agrees with Bi-terminated step edges [18], which, for the $BiAg_2$ stoichiometry, is only possible at fully kinked steps (average step direction rotated by 30°). Such tendency to terminate step edges with Bi is analogous to the 2D surfactant effect observed during Ag growth on Bi/Ag(111) [31], which is explained by the lower surface free energy of Bi ($\gamma_{0,Bi} = 0.53 \, J/m^2$) compared to that of Ag ($\gamma_{0,Ag} = 1.2 \, J/m^2$). To avoid zigzagging steps and favor parallel arrays at vicinal $BiAg_2$ surfaces, we use the c-Ag(111)$_{fk}$ sample with fully kinked steps oriented along the [11$\bar{2}$] direction. As shown in Figs. 1(d) and 1(e), the same 0.33 ML Bi evaporation and annealing process on c-Ag(111)$_{fk}$ leads to a radically different nanoscale morphology, with stoichiometric $BiAg_2$ terraces and straight, almost defect-free monatomic steps.

We carry out a systematic structural exploration of the $BiAg_2$ monolayer alloy across the c-Ag(111)$_{fk}$ substrate using LEED and STM and compare it to the pristine surface. The sharpness of the LEED pattern in the (111) position reveals accurate $BiAg_2$ stoichiometry of the topmost layer [Fig. 2(a)]. The top panels in Figs. 2(b) and 2(c) compare patterns acquired at an increasing vicinal angle before and after $BiAg_2$ alloy formation. In the pristine surface, the clear step-lattice splitting proves that regular monatomic step spacing is kept at all vicinal planes. Upon alloying, excellent $BiAg_2$ atomic-scale ordering is elucidated by the presence of sharp $(\sqrt{3} \times \sqrt{3})R30°$ spots that exhibit step-lattice splitting away from the (111) high-symmetry plane, as in the pristine surface. The step-lattice and $(\sqrt{3} \times \sqrt{3})R30°$-reconstruction nature of the diffracted electron beams is readily recognized in the LEED scans shown in the corresponding bottom panels. Each image is constructed with individual profiles along the line joining the $(-1,0)$ and $(-\frac{2}{3}, \frac{1}{3})$ spots (delimited by the red-dashed boxes above) from patterns acquired at 36 different vicinal angles (α). The clean substrate image presents two characteristic straight lines that converge at the (111) plane, as expected for a linear variation of the step density $1/d$, being $d = h/\sin\alpha$ the step spacing or terrace size, and h the step height [18]. In the $BiAg_2$ alloyed surface such step-related crossed lines appear replicated with the $(\sqrt{3} \times \sqrt{3})R30°$ periodicity, proving that the structural perfection in the step array is generally preserved. At $\alpha \sim 10°$ and $\alpha \sim 15°$ angles, that
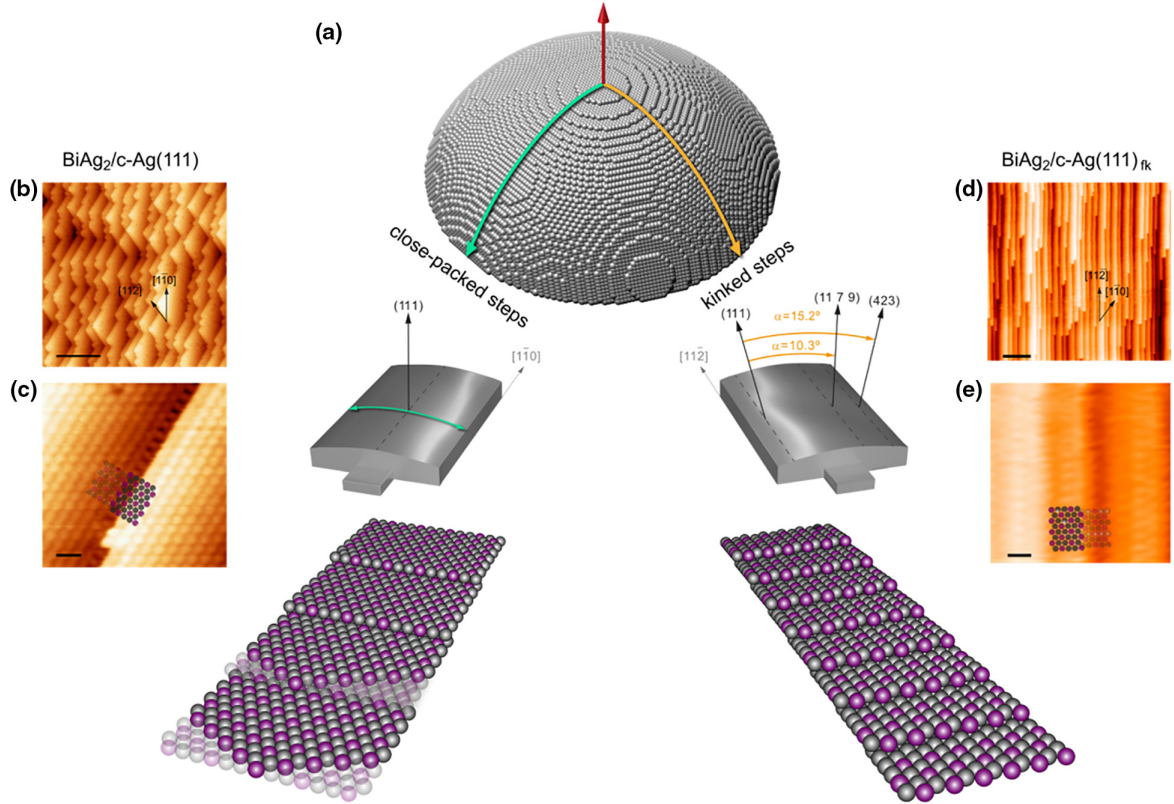
FIG. 1. Morphology of the $BiAg_2$ surface alloy on vicinal Ag(111) surfaces with different step types. (a) fcc-crystal sphere, marking close-packed (left) and fully kinked (right) vicinal surfaces explored for $BiAg_2$ growth through cylindrical sections (meridians on the sphere). Steps of close-packed surfaces reconstruct in Bi-terminated steps, as shown in the atomic model. In the c-Ag(111)$_{fk}$ fully kinked section we find the magic Ag(11 7 9) and Ag(423) vicinal orientations for $BiAg_2$ growth, tilted $\alpha = 10.3°$ and $\alpha = 15.2°$ away from the (111) plane, respectively. (b),(c) Room temperature STM images of stoichiometric $BiAg_2$ on the c-Ag(111)$_{cp}$ curved sample featuring close-packed steps ($\alpha = 5.2°$). The Bi termination of step edges drives the zigzagging transition into 120°-rotated fully kinked step segments (STM only resolves the Bi sublattice). (d),(e) Room temperature STM images of stoichiometric $BiAg_2$ on the c-Ag(111)$_{fk}$ curved sample ($\alpha = 8.8°$). The natural Bi termination of steps in this case favors long, defect-free straight steps.

is, near the (11 7 9) and (423) planes, all crossed lines nest with the respective step superlattice [red arrows in Fig. 2(c)]. At these angles, the very sharp oblique and rectangular LEED patterns strongly suggest that the two vicinal orientations indicated in Fig. 1(a) are accurately achieved. Beyond $\alpha \sim 18°$, Fig. 2(c) shows two sets of vertical diffraction streaks, indicating that surface alloying triggers the phase separation of sizable (735) ($\alpha = 18.1°$) and (312) ($\alpha = 22.2°$) $BiAg_2$ crystal facets.

The structural quality of the $BiAg_2$ step lattices grown onto the c-Ag(111)$_{fk}$ crystal is further examined by topographic STM analysis. The local fluctuations of the step spacing d around its average value $\langle d \rangle$, caused by the thermal excitation of kink atoms at stepped substrates, provides a good measure of the sharpness of the array [32,33]. The terrace-width fluctuation of the $BiAg_2$-covered vicinal surface of Fig. 1(d) is represented in the probability plot of Fig. 2(d). Using an automated line-by-line image analysis process [18], we obtain the statistical variation [$\mathbf{P}(d)$] of the terrace width d [also called terrace-width distribution] represented by the bar histogram (in red) of several images. It can be compared to the $\mathbf{P}(d)$ function of the bare vicinal plane (blue curve) measured at the same $\alpha \sim 6.2°$ vicinal angle (or mean value $\langle d \rangle = 2.2$ nm) [18]. After the formation of the alloy, the smooth $\mathbf{P}(d)$ curve

of the clean surface is broken up in a periodic series of sharply defined maxima, with periods equal to the Bi row spacing $\mathbf{a_0} = 0.42$ nm of the $(\sqrt{3} \times \sqrt{3})R30°$ reconstruction ($\mathbf{a_0} = \sqrt{3}\mathbf{a_{Ag}}$).

The radical step array transformation into $\mathbf{a_0}$ "quanta" is driven by the Bi termination of step edges and the precise $BiAg_2$ stoichiometry. The phenomenon is analogous to the one observed in bare vicinal Si(111) surfaces, where the 7×7 reconstruction pattern drives the terrace quantization and sharp termination of step edges [34,35], although in the present case self-organization also involves surface alloying. In Figs. 2(e) and 2(f) we show in a color scale α-dependent $\mathbf{P}(d)$ functions across the clean and the $BiAg_2$-covered c-Ag(111)$_{fk}$ surface. At the pristine sample [Fig. 2(e)], one can readily observe the characteristic evolution of the $\mathbf{P}(d)$ probability function as a function of α in vicinal metal surfaces [18,36], that is, the smooth transition from asymmetric-and-broad $\mathbf{P}(d)$ at large $\langle d \rangle$, to symmetric-and-sharp $\mathbf{P}(d)$ at small $\langle d \rangle$ where elastic step-step repulsion dominates. Upon $BiAg_2$ alloy formation [Fig. 2(f)], the $\mathbf{P}(d)$ plot histogram transforms in a set of vertical streaks, indicating that $\mathbf{a_0}$ quantization occurs at all vicinal planes along the curved surface. The terrace-width distribution map of Fig. 2(f) demonstrates the big advantage of using a curved sample for
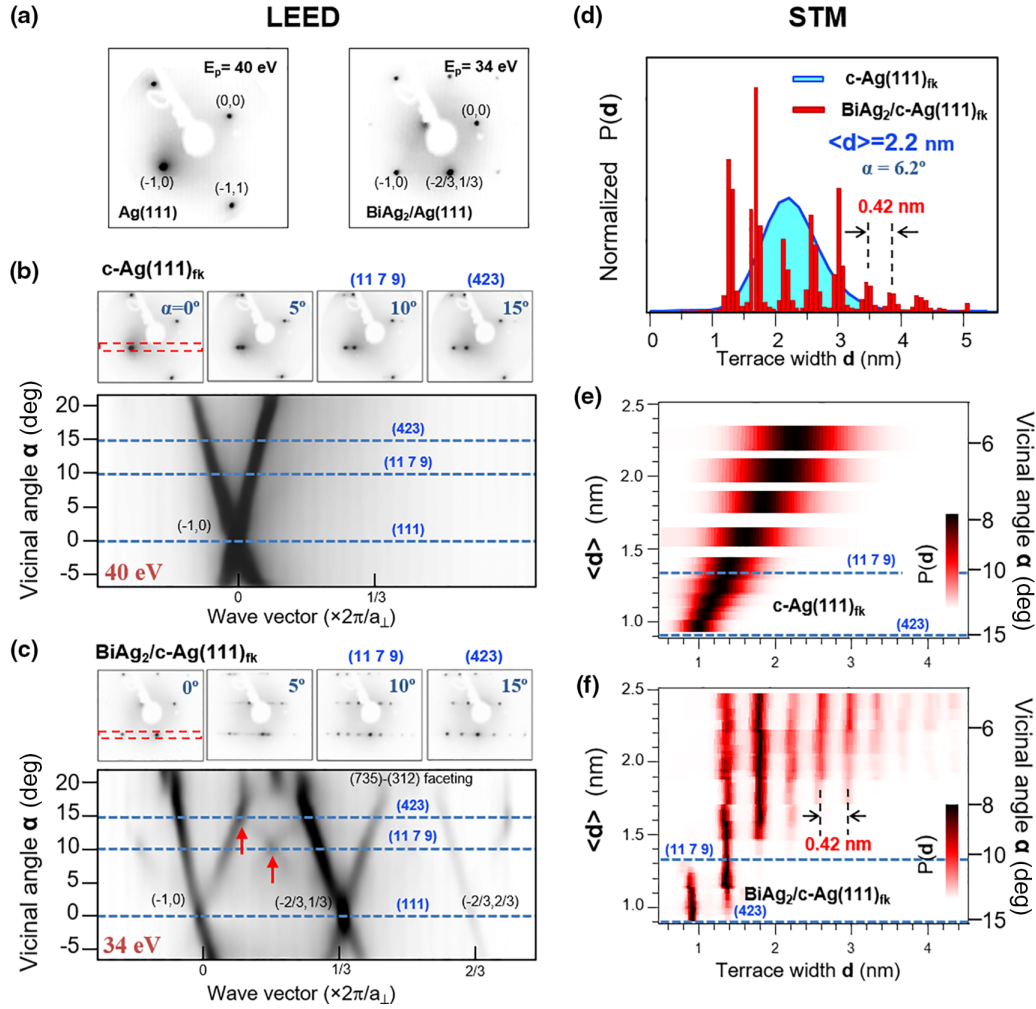
FIG. 2. Structural analysis of the fully kinked curved crystal before and after BiAg$_2$ alloy formation obtained at RT. (a) LEED pattern at the (111) plane prior and after alloy formation. (b) LEED at selected α angles on the clean c-Ag(111)$_{fk}$ sample. At $\alpha = 10°$ and $\alpha = 15°$ we probe the magic (11 7 9) and (423) planes, respectively. The bottom panel is a LEED image constructed with individual profiles containing the $(-1,0)$ spot, as marked by the red rectangle above. The straight crossing lines reflect the smoothly varying step density of the pristine curved surface. (c) Identical LEED analysis corresponding to the BiAg$_2$/c-Ag(111)$_{fk}$ system. The sharp $(\sqrt{3} \times \sqrt{3})R30°$ pattern indicates accurate BiAg$_2$ stoichiometry in all vicinal planes, particularly at selected (11 7 9) and (423) planes. The bottom panel corresponds to the LEED image constructed with individual profiles containing the $(-\frac{2}{3}, \frac{1}{3})$ spots, as marked by the red rectangle above. (d) Terrace-width distribution (TWD) analysis of STM images for 2.2 nm terraces ($\alpha \sim 6.2°$) of the pristine (blue) and BiAg$_2$ alloy on the c-Ag(111)$_{fk}$ curved crystal. The smooth histogram of the former is broken into 0.42 nm "quanta" in the latter, as expected for a BiAg$_2$ stoichiometry and Bi-terminated step edges (see text for details). (e),(f) Color plot of the TWD across the clean and the BiAg$_2$-covered c-Ag(111)$_{fk}$ crystal. Upon alloying, 0.42 nm quantization arises at all vicinal planes on the curved surface.

a proper identification of optimal surface orientations with sharp BiAg$_2$ step arrays [17,18,36]. In fact, the **P**(d) histogram notably sharpens for $\langle d \rangle$ values below ~ 1.5 nm ($\alpha \lesssim 9°$). Careful inspection pinpoints two vicinal planes at which the histogram presents a single **a$_0$** peak, namely, at $d = 1.36$ nm ($\alpha \sim 10°$) and $d = 0.93$ nm ($\alpha \sim 15°$). These angles correspond to the (11 7 9) and (423) Ag crystal planes, which may thus be defined as "magic" vicinal surfaces with *atomically sharp* step lattices, stabilized by the surface alloy structure.

Such magic planes in fact show up as sharply defined step arrays in the topographic STM images. In Fig. 3 we show representative STM images taken at these two selected positions on the curved surface, together with their respective histograms. These reveal BiAg$_2$ step grids of atomic-scale quality (black bars in the histogram), with a residual

presence of other terrace sizes at contiguous **a$_0$** quanta. The latter mostly are local fluctuations near the different "terrace" levels, which in turn reflect the $\sim 0.5°$ axis misorientation of the cylindrical sample. The **P**(d) histograms at the corresponding pristine surfaces are shown in red in the background and look quite sharp ($\sigma = \Delta d / \langle d \rangle \sim 0.3$). Moreover, the **P**($d$) histogram of the clean surface appears as the "envelope" of the respective BiAg$_2$ histogram, thereby restricting the appearance of BiAg$_2$ terrace quanta to those that fit in a $\Delta d = \sigma \langle d \rangle$ range around each $\langle d \rangle$. Or conversely, the terrace-size fluctuation σ of the clean vicinal substrate, which is connected to the Ag elastic properties, [32,33] ultimately determines the existence of atomically sharp (single **a$_0$** quantum) BiAg$_2$ step grids below a critical $\langle d \rangle = \mathbf{a_0}/\sigma \sim 1.4$ nm step spacing.
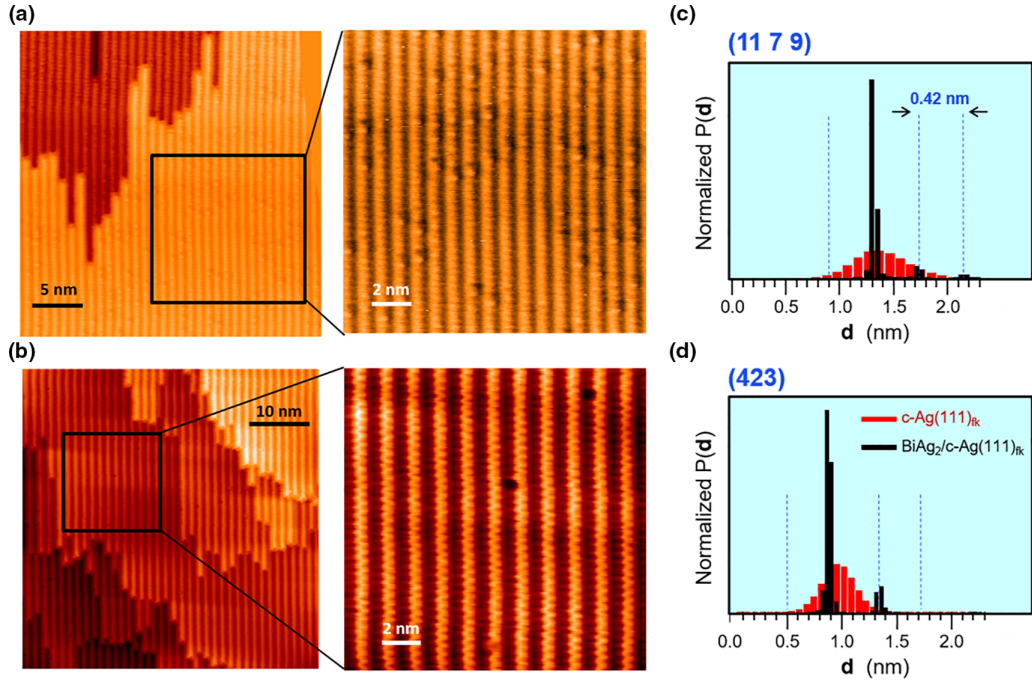
FIG. 3. 300 K STM topographic images from BiAg$_2$ surface alloy at the local (a) Ag(11 7 9) and (b) Ag(423) planes on the c-Ag(111)$_{fk}$ sample. Both positions exhibit sharp, almost defect-free monatomic step arrays. (c),(d) Terrace-width distribution (TWD) derived from statistical STM image analysis at BiAg$_2$/Ag(11 7 9) and BiAg$_2$/Ag(423) surfaces. The resulting surface alloy histograms (black) are compared with the TWD of their respective clean substrates (red). BiAg$_2$ growth leads to the almost complete elimination of terrace-size fluctuations around the expected d value of the ideal Ag(11 7 9) and Ag(423) crystal truncation planes.

The regular BiAg$_2$ step grids are of particular relevance for the exploration of Rashba state scattering via ARPES. Following the experimental arrangement of the photon beam and sample sketched in Fig. 4(a), we have investigated the Rashba band dispersion in the (111), (11 7 9), and (423) BiAg$_2$ surfaces, along the perpendicular (k_x) and parallel (k_y) directions of the step array. The main results are shown in Figs. 4(b) (direct photoemission) and 4(c) (second derivative), while further analysis of the curved sample at other orientations, isoenergetic k_x-k_y surfaces, as well as the light-polarization dependence are presented in Figs. S2–S5 [30]. At the (111) plane of the curved surface we observe the characteristic band manifold of BiAg$_2$, with the prominent split pair of occupied Rashba bands hybridizing with the partially unoccupied bands close to E_F [24]. At the (11 7 9) and (423) surfaces, coherent step-lattice scattering emerges, leading to radical changes in the band dispersion character in the direction perpendicular to the steps $E(k_x)$. The remarkable strength of such step scattering in BiAg$_2$ is noticed in the major affection of the band topology, which goes beyond the near-free electron subband replicas found for Shockley surface states in pristine vicinal noble metal substrates [17,18]. In contrast to the deeply modified $E(k_x)$ bands, in the direction parallel to the steps the downward $E(k_y)$ dispersion of the (111) plane is preserved, with no significant changes in group velocity for the higher-lying p_x band, and a consistent increase of about 35% from (111) to (423) in the lower-energy (inner) p_y band.

Due to the rich spin-orbital composition of BiAg$_2$ Rashba bands [25], their interaction with a step superlattice potential is expected to lead to a complex renormalization of the

orbital and spin textures, predominantly in the k_x direction. Such orbital/spin composition is determined by accurate DFT calculations for the (111), (11 7 9), and (423) BiAg$_2$ planes, represented in Figs. 4(d), 5, and S6–S9 [30]. All theoretical data correspond to the orbital and spin composition of the electronic states projected on Bi atoms, which are restricted in position to the surface plane. The ARPES bands in Fig. 4(c) can be compared with the orbital-resolved DFT bands of Fig. 4(d), where the experimental energy range is unshaded (full $p_x/p_y/p_z$ displayed in Fig. S6 [30]). Major features in the experimental bands are well reproduced in DFT calculations (note that the spread of the *ab initio* bands is an artifact derived from the finite slab used in the calculations). In this way, we can directly identify the orbital character of the ARPES features found in the three surfaces. Nevertheless, we focus our attention on the planar p_x and p_y components that dominate the Rashba bands and in the direction perpendicular to the step superlattice, as it is where the perturbations emerge.

A first clear observation in Figs. 4(b) and 4(c) is the predominance of p_y bands found for the vicinal surfaces. This can be attributed to their larger weight, according to the orbital-resolved theoretical band structure [Fig. 4(d)], and in addition to an experimental selection rule enhancement favoring the photoelectron emission from p_y (and p_z) orbital components in the horizontal polarization geometry of these measurements [cf. Fig. 4(a)]. Alternatively, we optimize the p_x orbital component when switching to vertical polarization (Fig. S5 [30]). Most importantly, we find drastic differences in the interaction with the step superlattice for the different in-plane orbital components. The p_y bands undergo a radical transformation
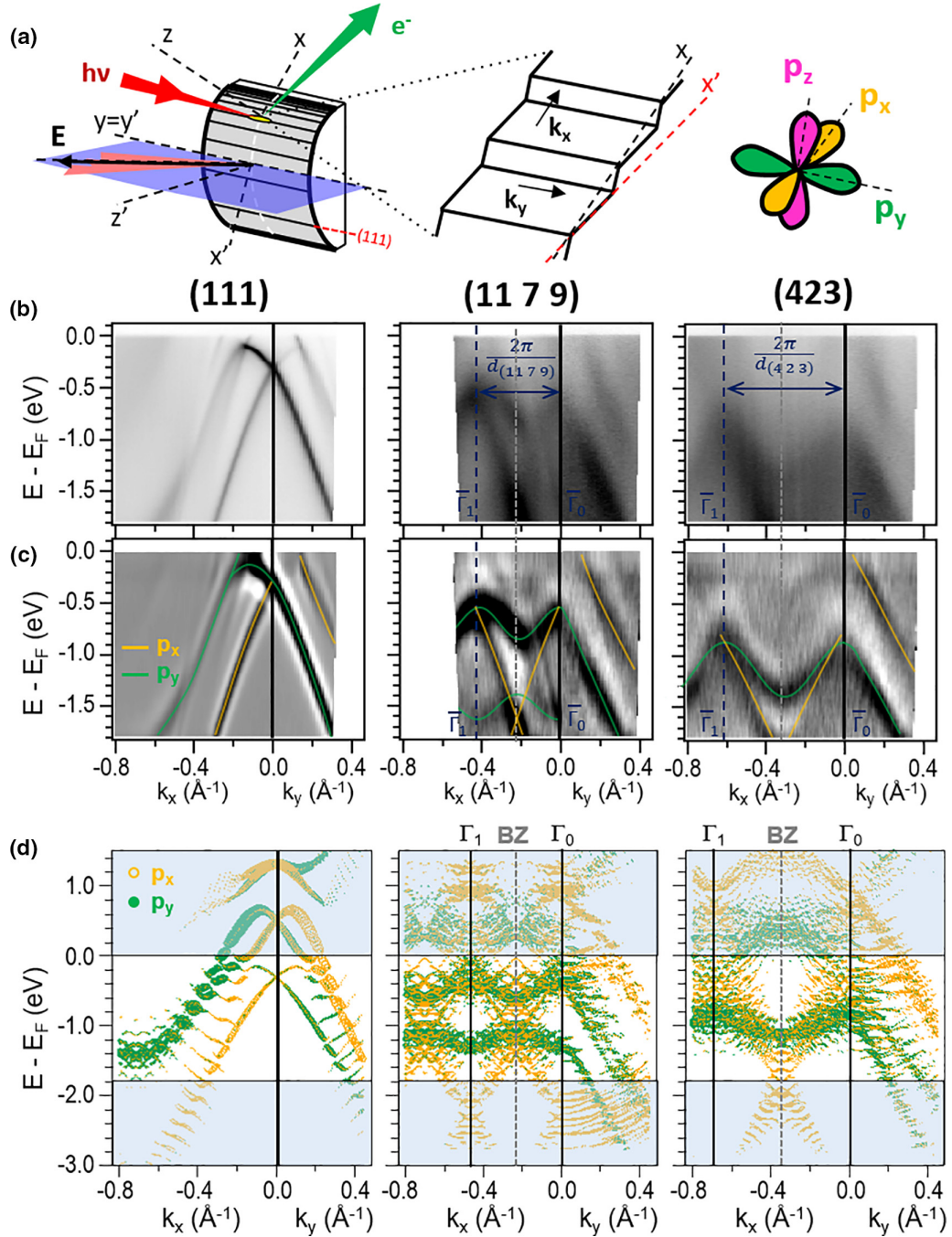
FIG. 4. Evolution of the electronic structure of Rashba helical states on the $BiAg_2/c\text{-}Ag(111)_{fk}$ curved surface. (a) Geometry of the ARPES experiment to determine the $E(k_x)$ band dispersion in the direction perpendicular to the steps. The light incidence angle is $45°$. For $E(k_y)$, the sample is rotated $90°$ around the z axis. The x' axis is directed along the terrace perpendicular to the steps, and the z' axis is perpendicular to the terrace. (b) ARPES intensity measured near the (111), (11 7 9), and (423) planes in the direction perpendicular (x) and parallel (y) to steps. For the (111) surface, these correspond to $\overline{\Gamma M}$ and $\overline{\Gamma K}$, respectively. The Brillouin zone edges, where bands are folded, are marked by vertical lines. (c) Second derivative of the photoemission intensity shown in (b). Green/yellow guidelines emulate the *ab initio* p_y/p_x bands of (d). (d) DFT-calculated p_y (green) and p_x (orange) projected electronic states. The dot size is proportional to the magnitude of the orbital projection. For clarity, data falling under 20% of the total intensity have been cut off. The energy range out of the $[−1.8, 0]$ eV explored in ARPES appears shaded.

in the $\overline{\Gamma X}$ direction, becoming subbands that are backfolded by the step superlattice and are separated by energy gaps. In the experimental energy range explored, and for the photon energy chosen here [37], two of these subbands are found for the (11 7 9) surface, and one for the (423) surface, in

very good agreement with the DFT results. Moreover, the strong interaction of these states with the step superlattice leads to a renormalization of p_y bands beyond the nearly free-electron scenario, with the formation of large energy gaps and the inversion of the effective mass. In stark contrast, the
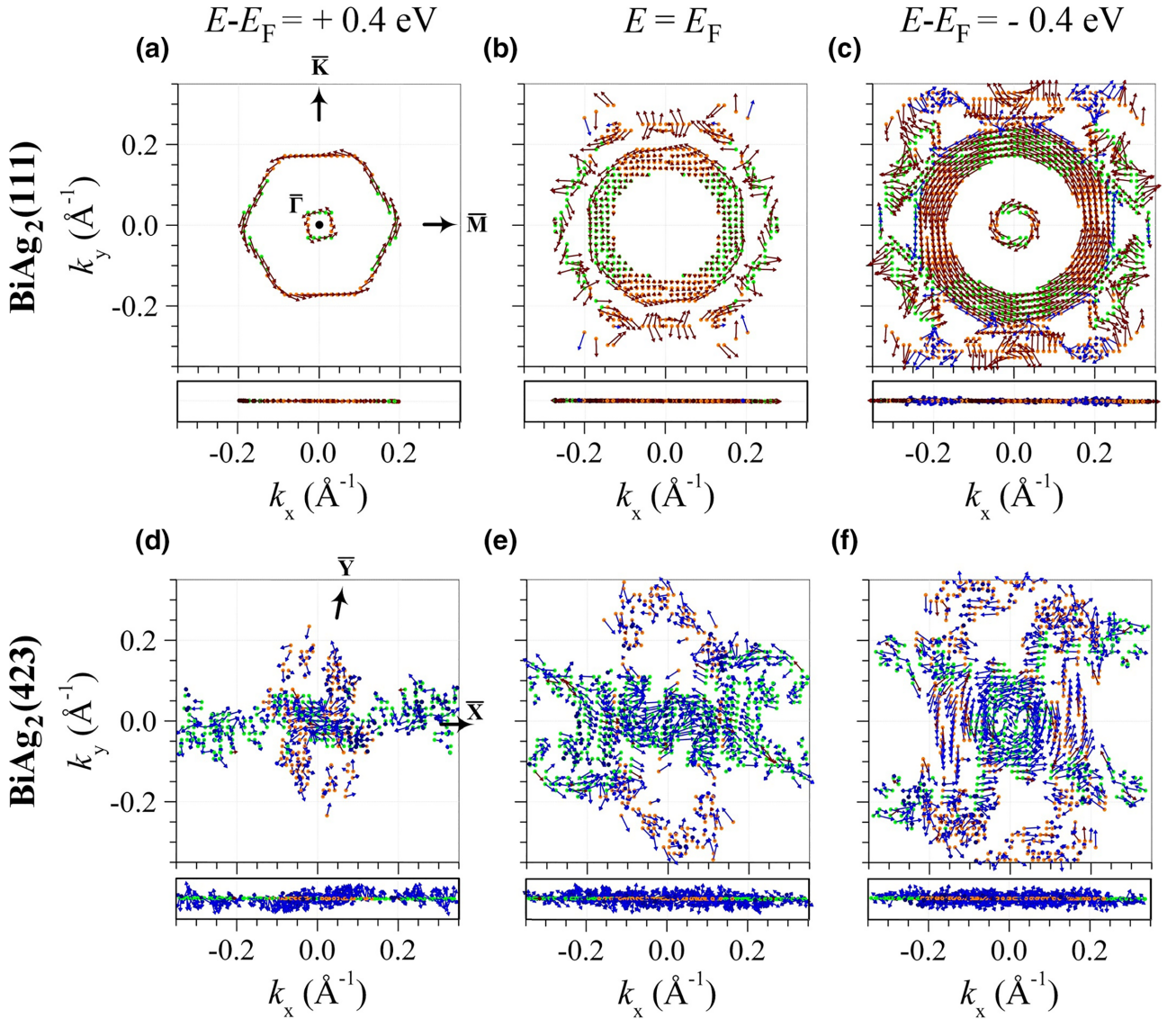
FIG. 5. Spin texture of Rashba helical states of BiAg$_2$ at the flat (111) (top) and vicinal (423) (bottom) surfaces on isoenergetic k_x-k_y planes with energies of +0.4 eV (a), 0 eV (b), and −0.4 eV (c). Orange dots show bands formed predominantly by p_x orbitals and green dots show bands formed predominantly by p_y orbitals. Brown arrows indicate spin moments lying in the surface plane [$\vec{S} = (S_x, S_y, 0)$]. Spin moments deviating from the surface plane (with a nonzero S_z component) are indicated by the blue arrows. The bottom rectangular panels evidence the presence of electron spin momentum along the z axis for the step superlattices.

dominant effect of the step superlattice on p_x bands is the backfolding induced by the larger unit cell (see Fig. S7 [30]), with no sizable signature of interactions. The overall analysis clearly shows that the scattering of the Rashba helical states of the flat surface on the steps of the vicinal surfaces leads to the separation, both in energy and in k space, of the states formed mainly by p_x orbitals from those formed mainly by p_y orbitals (see also Figs. 5 and S7–S9). The orbital-selective perturbations of bands are reproduced in the calculations not considering the spin-orbit coupling (Fig. S8 [30]), thus the selective scattering must be attributed to other effects, such as the different surface localization of the BiAg$_2$ bands. Indeed, artificial resonators built on flat BiAg$_2$ surfaces reveal that in the $\overline{\Gamma X}$ direction ($\overline{\Gamma M}$ in the flat surface) the p_y branch of the unoccupied ($m_j = 1/2$) bands is more localized on the Bi plane than the p_x branch of the occupied band, and the

spin-flip scattering mechanism found for the former is most effective in the Bi-terminated steps of our superlattice [25].

The evolution of the 3D spin texture of Rashba bands from the flat BiAg$_2$(111) plane to the stepped surfaces is difficult to visualize in 2D plots. To facilitate this task, in Fig. 5 we represent for the (111) and (423) surfaces the three-dimensional spin vectors of the Rashba states for isoenergetic cross sections at three different energies: $E-E_F = 0.4$, 0.0, and −0.4 eV (see Fig. S9 [30] to compare the superlattice effect with the simple folding of the unit cell of the flat surface). In the flat surface [Figs. 5(a)–5(c)], we find the in-plane orthogonal relation between spin and crystal momentum that is characteristic of helical Rashba states. That is, the spin projection is purely $S_y(S_x)$ in the $k_x(k_y)$ directions, respectively, with negligible S_z contribution in both cases. The transition to the vicinal surface shows a dramatic rearrangement of both the isoenergetic cross

section of the band spectrum and its spin texture [Figs. 5(d)–5(f)]. The orbital-selective interaction already discussed leads to a separation of predominantly p_x and p_y type states. The spin texture of both orbital components reveals a strong deviation from the in-plane helical configuration of the flat surface, with significant contribution of the out-of-plane S_z component and a nonhelical S_x-S_y distribution.

The appearance of out-of-plane components of the spin texture is related to the Rashba-type spin splitting. In adsorbed atoms, the rotation of the polarization vector from in-plane to out-of-plane direction has been attributed to the appearance of a large anisotropy in the partial charge distribution [38,39]. In our case, the difference in the binding of Bi atoms on the step and on the terrace to their nearest neighbors leads to different directions of polarization of these atoms due to the anisotropic valence charge distribution. As a result, a potential gradient arises on the vicinal surface, and hence an electric field with both in-plane and out-of-plane components, which, acting on the electrons in the surface bonds, lead to different spin polarization orientations. Also note that a transition to noncoplanar spin texture has been reported for a Pb-based Rashba superlattice, and attributed to a matching between Fermi nesting and momentum splitting of the bands that leads to the emergence of spin-orbit density waves [5]. Such coincidence in momentum space cannot simultaneously exist in the two superlattice periods studied here when assuming the direct folding of rigid bands (umklapps). Contrarily, the here reported complex orbital-selective band renormalization found in the BiAg$_2$ superlattice is far from the backfolded rigid band picture, and hence understanding the origin of these noncoplanar spin textures of vicinal BiAg$_2$ surfaces merits further investigation.

III. CONCLUSIONS

In summary, we have shown that by using a curved Ag crystal featuring a smoothly variable density of kinked steps, we can tune the growth of the BiAg$_2$ monolayer alloy characterized by straight, Bi-terminated steps of tunable density. We achieve sharp arrays exhibiting magic monoatomic step periodicities whenever integer numbers of the BiAg$_2$ unit cell fit within small average terrace sizes (below $\langle d \rangle \sim 1.4$ nm or $\alpha > 9°$). ARPES experiments demonstrate that scattering at the step potential superlattice leads to a pronounced, orbital-selective band topology renormalization where the effect of strong repulsive scattering at the steps is mainly observed for p_y bands. On top of that, the step superlattice drives the system to a strong reconfiguration of the spin texture, bringing the spin out of its original in-plane helical configuration. Overall, our results demonstrate the potential of well-defined step superlattices to engineer helical bands not only in terms of the energy dispersion, but also in its spin-orbital texture. Other surface alloys expected to feature similar exciting properties, such as PbAg$_2$, BiCu$_2$, etc., could be synthesized following an analogous approach, namely, epitaxy on curved surfaces with kinked steps. Because these share the same stoichiometry, the same peculiar growth procedure should hold; that is, the segregation of the heavy element to the steps and the lattice matching with the reconstructed surface.

IV. METHODS

The curved crystal surfaces of Ag were prepared by repeated cycles of sputtering, with Ar$^+$ at an energy of 1 keV and incidence angle of 45° in the direction parallel to steps, followed by a mild annealing to 700 K for 15 min at a maximum pressure of 1×10^{-9} mbar. Both c-Ag(111)$_{fk}$ and c-Ag(111)$_{cp}$ were fabricated (BihurCrystal Ltd., Spain) by mechanical erosion and polishing of (645)- and (111)-oriented Ag wafers, such as to define 24° and 16° cylindrical sectors, with axis parallel to the [11$\bar{2}$] and [1$\bar{1}$0] crystal directions, respectively. The c-Ag(111)$_{fk}$ sample was mainly used in the present work, whereas the c-Ag(111)$_{cp}$ sample (yielding the BiAg$_2$ zigzag steps) featured close-packed pristine steps with variable densities of A type ({100}-like minifacets) and B type ({111}-like minifacets) and was mainly used for comparative STM experiments (see Fig. S1 [30]).

Bi was evaporated from a Knudsen cell using rates of the order of 0.06 ML/min with the sample held at 300 K, and then a gentle post-annealing at 550 K results in optimal formation of the BiAg$_2$ monolayer alloy. For STM and LEED experiments, we ensure the accurate BiAg$_2$ stoichiometry by evaporating, at 300 K, a shallow 0.2-0.4 monolayer wedge in the direction parallel to the steps, and then selecting the precise 0.33 ± 0.02 Bi ML position on the sample, as judged from LEED. For ARPES experiments, a quartz-microbalance calibration is previously obtained to achieve a direct 0.33 ML evaporation for the experiment. The quality of the surface alloy is further checked by considering the sharpness of the spin-orbit split bands at the (111) plane and through comparison with the expected LEED patterns.

LEED measurements were conducted at 300 K, using a standard three-grid optics system (Omicron). Specific points on the c-Ag(111)$_{fk}$ curved sample were addressed with the minimum 300 μm spot size, which spreads over a $\Delta\alpha \sim 0.35°$ arc on the curved surface. Such spreading of the electron beam explains the spot-splitting broadening observed in LEED images from the bare c-Ag(111)$_{fk}$ [see Fig. 2(a)].

STM imaging was carried out using a variable temperature setup (Omicron) operating at 300 K. The tunneling current was set to $\sim$0.1 nA, and the sample bias to either -1.0 or $+1.1$ V. To elaborate the probability $\mathbf{P}(d)$ histograms, STM images were acquired at the selected surface areas exhibiting homogeneous step arrays in the micrometer scale. Topography data were analyzed using a home-programmed code that automatically finds step edges and delivers the $\mathbf{P}(d)$ histogram for each image [18]. The $\mathbf{P}(d)$ data shown in Figs. 2 and 3 correspond either to a single or to the average of two contiguous STM frames, where sizes vary between 40×40 and 300×300 nm^2, in order to image between 20 and 40 steps within the same frame.

ARPES measurements were performed at the CASSIOPEE beamline of SOLEIL Synchrotron (Saint-Aubin, France). We used linearly polarized photons of 21 eV and a hemispherical electron analyzer with vertical slits with $\pm15°$ angular acceptance, which provides high-resolution band mapping by moving the polar angle of the manipulator, so that z' is always contained within the light incidence plane shaded in Fig. 4(a). The photon beam impinged on the sample with a 45° angle. The spot size on the sample was $\sim$50 $\times$ 15 μm^2, with the wider

axis aligned parallel to the steps. The 15 μm length perpendicular to the step direction defined a negligible 0.02° spread over the curve of the crystal, yielding sharp sensitivity to the local crystallographic orientation. The ARPES experiments were carried out at low temperature (100 K) and the angle and energy resolutions were set to 0.05° and 10 meV, respectively. In this ARPES geometry, the (horizontal) light-polarization vector is contained in the sample's y-z' plane that coincides with the direction parallel to the step. Unfortunately, spin-resolved ARPES cannot be attempted with this curved sample due to the limitation in the spread over the surface curvature that would further smear out the already complex structure.

Density functional theory calculations were performed using the projector augmented-wave potentials [39] implemented in the Vienna *ab initio* simulation package [40–42]. The exchange-correlation energy was treated using the generalized gradient approximation of Perdew *et al.* [43]. Scalar relativistic corrections and spin-orbit coupling were included by the second variation method [44]. The (423) and (11 7 9) vicinal surfaces, as well as the nonvicinal (111), were modeled by an asymmetric slab, consisting, respectively, of 27, 20, and 27 atomic layers of Ag, with one surface covered with the monolayer of the $(\sqrt{3} \times \sqrt{3})R30°$ BiAg$_2$ surface alloy. We optimized the positions of the atoms in the outermost eight layers. All structural optimizations were performed using a force-tolerance criterion for convergence of 0.01 eV/Å. The cutoff energy for the plane-wave basis was set to 250 eV. For self-consistent calculations, the Brillouin zone of the (423), (11 7 9) and (111) films was sampled with the $3 \times 5 \times 1$, $2 \times 5 \times 1$, and $5 \times 5 \times 1$ k-point mesh, respectively. In the surface band structures, we considered states that have more than 8% charge in the surface Bi and Ag atoms as surface states.

[1] G. Bihlmayer, P. Noël, D. V. Vyalikh, E. V. Chulkov, and A. Manchon, Rashba-like physics in condensed matter, Nat. Rev. Phys. **4**, 642 (2022).

[2] A. Manchon, H. C. Koo, J. Nitta, S. M. Frolov, and R. A. Duine, New perspectives for Rashba spin–orbit coupling, Nat. Mater. **14**, 871 (2015).

[3] D. Go, J.-P. Hanke, P. M. Buhl, F. Freimuth, G. Bihlmayer, H.-W. Lee, Y. Mokrousov, and S. Blügel, Toward surface orbitronics: Giant orbital magnetism from the orbital Rashba effect at the surface of sp-metals, Sci. Rep. **7**, 46742 (2017).

[4] V. Y. Demikhovskii and D. V. Khomitsky, Spin-orbit lateral superlattices: Energy bands and spin polarization in 2DEG, JETP Lett. **83**, 340 (2006).

[5] C. Brand, H. Pfnür, G. Landolt, S. Muff, J. H. Dil, T. Das, and C. Tegenkamp, Observation of correlated spin–orbit order in a strongly anisotropic quantum wire system, Nat. Commun. **6**, 8118 (2015).

[6] P. Kleinert, V. V. Bryksin, and O. Bleibaum, Spin accumulation in lateral semiconductor superlattices induced by a constant electric field, Phys. Rev. B **72**, 195311 (2005).

[7] D. V. Khomitsky, Manipulating the spin texture in a spin-orbit superlattice by terahertz radiation, Phys. Rev. B **77**, 113313 (2008).

[8] D. C. Marinescu and F. Lung, Rashba-enhanced plasmon in a two-dimensional lateral superlattice, Phys. Rev. B **82**, 205322 (2010).

[9] Y. Lu, W.-Y. He, D.-H. Xu, N. Lin, and K. T. Law, Platform for engineering topological superconductors: Superlattices on Rashba superconductors, Phys. Rev. B **94**, 024507 (2016).

[10] V. Mourik, K. Zuo, S. M. Frolov, S. R. Plissard, E. P. A. M. Bakkers, and L. P. Kouwenhoven, Signatures of Majorana fermions in hybrid superconductor-semiconductor nanowire devices, Science **336**, 1003 (2012).

[11] A. Mugarza and J. E. Ortega, Electronic states at vicinal surfaces, J. Phys.: Condens. Matter **15**, S3281 (2003).

[12] A. Mugarza, A. Mascaraque, V. Pérez-Dieste, V. Repain, S. Rousset, F. J. García de Abajo, and J. E. Ortega, Electron confinement in surface states on a stepped gold surface revealed by angle-resolved photoemission, Phys. Rev. Lett. **87**, 107601 (2001).

[13] A. Mugarza, A. Mascaraque, V. Repain, S. Rousset, K. N. Altmann, F. J. Himpsel, Yu. M. Koroteev, E. V. Chulkov, F. J. García de Abajo, and J. E. Ortega, Lateral quantum wells at vicinal Au(111) studied with angle-resolved photoemission, Phys. Rev. B **66**, 245419 (2002).

[14] R. Losio, K. N. Altmann, and F. J. Himpsel, Continuous transition from two- to one-dimensional states in Si(111)-(5 × 2)-Au, Phys. Rev. Lett. **85**, 808 (2000).

[15] I. Barke, F. Zheng, T. K. Rügheimer, and F. J. Himpsel, Experimental evidence for spin-split bands in a one-dimensional chain structure, Phys. Rev. Lett. **97**, 226405 (2006).

[16] J. E. Ortega, A. Mugarza, V. Repain, S. Rousset, V. Pérez-Dieste, and A. Mascaraque, One-dimensional versus two-dimensional surface states on stepped Au(111), Phys. Rev. B **65**, 165413 (2002).

[17] J. E. Ortega, M. Corso, Z. M. Abd-el-Fattah, E. A. Goiri, and F. Schiller, Interplay between structure and electronic states in step arrays explored with curved surfaces, Phys. Rev. B **83**, 085411 (2011).

[18] J. E. Ortega, G. Vasseur, I. Piquero-Zulaica, S. Matencio, M. A. Valbuena, J. E. Rault, F. Schiller, M. Corso, A. Mugarza, and J. Lobo-Checa, Structure and electronic states of vicinal Ag(111) surfaces with densely kinked steps, New J. Phys. **20**, 73010 (2018).

[19] C.-H. Park, L. Yang, Y.-W. Son, M. L. Cohen, and S. G. Louie, Anisotropic behaviours of massless Dirac fermions in graphene under periodic potentials, Nat. Phys. **4**, 213 (2008).

[20] J. Lobo-Checa, F. Meier, J. H. Dil, T. Okuda, M. Corso, V. N. Petrov, M. Hengsberger, L. Patthey, and J. Osterwalder, Robust spin polarization and spin textures on stepped Au(111) surfaces, Phys. Rev. Lett. **104**, 187602 (2010).

[21] C. Tegenkamp, T. Ohta, J. L. McChesney, H. Dil, E. Rotenberg, H. Pfnür, and K. Horn, Coupled Pb chains on Si(557): Origin of one-dimensional conductance, Phys. Rev. Lett. **100**, 076802 (2008).

[22] C. Tegenkamp, D. Lükermann, H. Pfnür, B. Slomski, G. Landolt, and J. H. Dil, Fermi nesting between atomic wires with strong spin-orbit coupling, Phys. Rev. Lett. **109**, 266401 (2012).

[23] T. Das, Spin-orbit density wave induced hidden topological order in URu_2Si_2, Sci. Rep. **2**, 596 (2012).

[24] C. R. Ast, J. Henk, A. Ernst, L. Moreschini, M. C. Falub, D. Pacilé, P. Bruno, K. Kern, and M. Grioni, Giant spin splitting through surface alloying, Phys. Rev. Lett. **98**, 186807 (2007).

[25] S. Schirone, E. E. Krasovskii, G. Bihlmayer, R. Piquerel, P. Gambardella, and A. Mugarza, Spin-flip and element-sensitive electron scattering in the $BiAg_2$ surface alloy, Phys. Rev. Lett. **114**, 166801 (2015).

[26] H. Hirayama, Y. Aoki, and C. Kato, Quantum interference of Rashba-type spin-split surface state electrons, Phys. Rev. Lett. **107**, 027204 (2011).

[27] L. El-Kareh, P. Sessi, T. Bathon, and M. Bode, Quantum interference mapping of Rashba-split Bloch states in Bi/Ag(111), Phys. Rev. Lett. **110**, 176803 (2013).

[28] G. Bihlmayer, S. Blügel, and E. V. Chulkov, Enhanced Rashba spin-orbit splitting in BiAg (111) and PbAg (111) surface alloys from first principles, Phys. Rev. B **75**, 195414 (2007).

[29] J. E. Ortega, J. Lobo-Checa, G. Peschel, S. Schirone, Z. M. Abd El-Fattah, M. Matena, F. Schiller, P. Borghetti, P. Gambardella, and A. Mugarza, Scattering of surface electrons by isolated steps versus periodic step arrays, Phys. Rev. B **87**, 115425 (2013).

[30] See Supplemental Material at http://link.aps.org/supplemental/10.1103/PhysRevB.109.125427 for a complete set of STM images, additional bands, constant energy surfaces and light-polarization analysis in ARPES, and extended and complementary DFT calculations and theoretical discussions.

[31] H. Fukumoto, M. Miyazaki, Y. Aoki, K. Nakatsuji, and H. Hirayama, Initial stage of Ag growth on Bi/Ag(111)$\sqrt{3} \times \sqrt{3}$ surfaces, Surf. Sci. **611**, 49 (2013).

[32] T. L. Einstein, Using the Wigner–Ibach surmise to analyze terrace-width distributions: History, user's guide, and advances, Appl. Phys. A **87**, 375 (2007).

[33] E. D. Williams and N. C. Bartelt, Thermodynamics of surface morphology, Science **251**, 393 (1991).

[34] A. Kirakosian, R. Bennewitz, J. N. Crain, Th. Fauster, J.-L. Lin, D. Y. Petrovykh, and F. J. Himpsel, Atomically accurate Si grating with 5.73 nm period, Appl. Phys. Lett. **79**, 1608 (2001).

[35] J. Viernow, J.-L. Lin, D. Y. Petrovykh, F. M. Leibsle, F. K. Men, and F. J. Himpsel, Regular step arrays on silicon, Appl. Phys. Lett. **72**, 948 (1998).

[36] A. L. Walter, F. Schiller, M. Corso, L. R. Merte, F. Bertram, J. Lobo-Checa, M. Shipilin, J. Gustafson, E. Lundgren, A. X. Brión-Ríos, P. Cabrera-Sanfelix, D. Sánchez-Portal, and J. E. Ortega, X-ray photoemission analysis of clean and carbon monoxide-chemisorbed platinum(111) stepped surfaces using a curved crystal, Nat. Commun. **6**, 8903 (2015).

[37] At other photon energies, and in contrast to the almost-constant photon-energy dependence of the Rahsba bands in the (111) plane, we detect strong spectral density variations in the (11 7 9) and (423) surfaces, which are related to the broad spectral distribution and mixing of all states.

[38] M. Krawiec, M. Kopciuszyński, and R. Zdyb, Different spin textures in one-dimensional electronic bands on Si(553)-Au surface, Appl. Surf. Sci. **373**, 26 (2016).

[39] M. Kopciuszyński, M. Krawiec, R. Zdyb, and M. Jałochowski, Purely one-dimensional bands with a giant spin-orbit splitting: Pb nanoribbons on Si(553) surface, Sci. Rep. **7**, 46215 (2017).

[40] P. E. Blöchl, Projector augmented-wave method, Phys. Rev. B **50**, 17953 (1994).

[41] G. Kresse and D. Joubert, From ultrasoft pseudopotentials to the projector augmented wave method, Phys. Rev. B **59**, 1758 (1999).

[42] G. Kresse and J. Furthmüller, Efficient iterative schemes for *ab initio* total-energy calculations using a plane-wave basis set, Phys. Rev. B **54**, 11169 (1996).

[43] J. P. Perdew, K. Burke, and M. Ernzerhof, Generalized gradient approximation made simple, Phys. Rev. Lett. **77**, 3865 (1996).

[44] D. D. Koelling and B. N. Harmon, A technique for relativistic spin-polarized calculations, J. Phys. C: Solid State Phys. **10**, 3107 (1977).